Buoyant force and sinking conditions of a hydrophobic thin rod floating on water

Jian-Lin Liu,[1] Xi-Qiao Feng,[1,*] and Gang-Feng Wang[2]
[1]*FML, Department of Engineering Mechanics, Tsinghua University, Beijing 100084, China*
[2]*Department of Engineering Mechanics, Xi'an Jiaotong University, Xi'an 710049, China*
(Received 14 July 2007; revised manuscript received 16 September 2007; published 13 December 2007)

Owing to the superhydrophobicity of their legs, such creatures as water striders and fisher spiders can stand effortlessly, walk and jump quickly on water. Directed toward understanding their superior repellency ability, we consider hydrophobic thin rods of several representative cross sections pressing a water surface. First, the shape function of the meniscus surrounding a circular rod is solved analytically, and thereby the maximal buoyant force is derived as a function of the Young's contact angle and the rod radius. Then we discuss the critical conditions for a rod to sink into water, including the maximal volume condition and the meniscus-contact condition. Furthermore, we study the sinking conditions and the maximal buoyant forces of hydrophobic long rods with elliptical, triangular, or hexagonal cross-section shapes. The theoretical solutions are quantitatively consistent with existing experimental and numerical results. Finally, the optimized structures of water strider legs are analyzed to elucidate why they can achieve a very big buoyant force on water.

DOI: 10.1103/PhysRevE.76.066103 PACS number(s): 87.68.+z, 68.08.−p

I. INTRODUCTION

Such animals as fisher spiders and water striders have the striking feats to float, walk, and jump on the water surfaces of ponds, rivers, and even open oceans [1–3]. Much attention has been attracted in the past decades on the locomotion mechanisms of these creatures [4–9]. Their extremely strong repellency ability has been attributed to the hierarchical microstructures and nanostructures of their legs with a large contact angle [10,11], because roughness on a solid surface can enhance its superhydrophobic behavior [12–14]. Experimental measurements found that a single leg of water strider can provide a supporting force about 15 times the total body weight, and the corresponding volume of water ejected is 300 times that of the leg [10]. Another interesting experiment shows that the water-supporting force of a single leg of the mosquito is about 23 times its body weight [15]. Inspired also by the leaves of louts and Lady's Mantle, superhydrophobic surfaces have been created by chemical modification and/or introducing hierarchical surface structures [16–18]. By mimicking water strider legs, recently, Shi *et al.* [19,20] produced a gold rod with superhydrophobic property and measured the maximal buoyant force of the rod.

When an object is brought into contact with a liquid surface, an upward or downward meniscus forms around its edge. The meniscus profiles in different situations have been analytically or numerically studied by solving the Laplace equation of liquid surfaces [21–23]. Due to the meniscus or capillary effect, the surface tension of a liquid provides a buoyant force large enough to float small objects denser than the liquid, which seemingly violates Archimedes' principle [24]. Capillary interaction may also drive solid components floating at interfaces to self-assemble [25,26]. The buoyant force of a floating object can be directly integrated from the liquid volume displaced by the body and the meniscus, but the critical sinking condition of a floating object has not been well recognized. In order to explain their experimental results, Trompette *et al.* [27] assumed that a spherical particle will sink when one-half of the particle surface is wetted by the liquid. Hu *et al.* [9] adopted an approximate estimation of the buoyant force for a very thin cylinder rod by ignoring the rod volume. Besides, Penner [28] thought that a floating disk will pierce into water when the direction of the surface tension becomes vertical. The sinking conditions of a cylinder rod, a disk and a sphere were also determined when the extruded volume of water amounts to the maximum value [29–33]. To analyze the buoyant force of a water strider leg, very recently, Feng *et al.* [11] adopted another roughly approximate sinking condition when the two bulging points of the menisci contact with each other, as suggested previously by Rapacchietta *et al.* [29]. Despite the previous calculations of the buoyant force, the critical condition of a rod sinking into water remains an extensively argued but as yet unsolved issue. The dependence relationships between the buoyant force and the characteristic size and cross-section shape of the rod have not been quantitatively deciphered either.

In order to gain an insight of the striking repellency behavior of such insects as water striders [10,11], we here analyze the buoyant force and sinking condition of hydrophobic thin rods of different cross-section shapes floating on water. First, the shape of the meniscus surrounding a circular rod is analytically solved from the Laplace equation, and thereby the buoyant force is calculated by integrating the total water volume extruded by the rod. Then the critical sinking conditions of a long rod are discussed. Moreover, we compare quantitatively the buoyant forces of rods with elliptical, triangular, and hexagonal cross sections. The optimization problem on the cross section of water strider legs to attain a large buoyant force is addressed.

II. BUOYANT FORCE AND SINKING CONDITION OF A THIN CIRCULAR ROD

A. Meniscus shape

We first consider a smooth thin cylinder of circular cross section floating on a liquid surface. Let θ_Y denote the mac-

*Corresponding author. fengxq@tsinghua.edu.cn. FAX: +86-10-62781824.

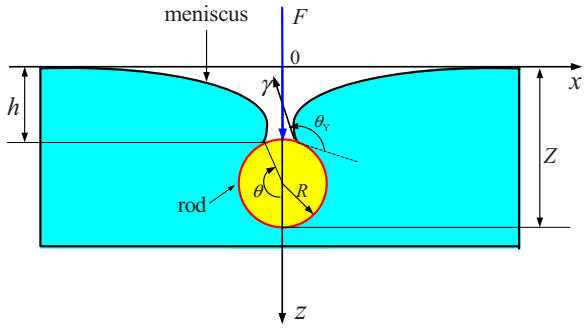

FIG. 1. (Color online) A circular rod floating on water and subjected to a pressing force F.

roscopically effective contact angle of the cylinder, which is a function of the chemical compositions and surface microstructures [10,11]. The meniscus around the rod may be upward or downward with respect to the original horizontal liquid surface, depending on whether the cylinder is hydrophilic or hydrophobic. Here, we investigate only the hydrophobic case ($\theta_Y > 90°$), though the hydrophilic case can be analyzed analogously. The length L of the cylinder is assumed to be much greater than its radius R (e.g., $L > 30R$). In this case, the three-dimensional end effect is negligible, and thus the problem reduces to a two-dimensional one. Refer to a Cartesian coordinate system (o-xz), as shown in Fig. 1, where F is an externally applied force on per unit length of the cylinder, and 2θ is the sector angle of the wetted part of the cylinder surface. As the force F increases, the rod will press gradually the water surface and correspondingly the angle θ increases. For a relatively smaller θ, the shape function $z=z(x)$ of the meniscus is monotonic and single valued with respect to the coordinate x, while for θ larger than $3\pi/2-\theta_Y$, there will be an inflection point, as shown in Fig. 1. With the increase in the force F, the triple contact line moves along the rod surface but the contact angle between the solid and the liquid surfaces is assumed to keep a constant, θ_Y. Only quasistatic processes are considered here, and then no effect of dynamics is accounted for.

Across the liquid-vapor interface, there exists a Laplace pressure difference,

$$\Delta p = p_L - p_V = \rho_L g z, \tag{1}$$

where p_L and p_V are the pressures in the liquid and vapor, respectively, ρ_L is the mass density of the liquid, and g is the acceleration of gravity. Due to the possible presence of an inflection point, the shape function of the meniscus is expressed by the function $x=x(z)$, which is always single valued. The Laplace pressure difference $\Delta p=\rho_L g z$ depends upon the average curvature of the meniscus via the classical Laplace equation [34]

$$x''(1+x'^2)^{-3/2} = \kappa^2 z, \tag{2}$$

where the apostrophe stands for the derivative with respect to the coordinate z, $\kappa^{-1}=\sqrt{\gamma/(\rho_L g)}$ is the capillary length, and γ is the surface tension of the liquid. The solution of Eq. (2) is

$$x' = \left(\frac{1}{2}\kappa^2 z^2 - c_1\right)\left[1 - \left(\frac{1}{2}\kappa^2 z^2 - c_1\right)^2\right]^{-1/2}, \tag{3}$$

with c_1 being an integration constant. The boundary conditions of the infinite liquid surface are $x \to +\infty$ and $x' \to -\infty$ for $z \to 0$. Then it is determined from Eq. (3) that $c_1=1$. So the meniscus profile satisfies the following equation:

$$x' = \frac{z^2 - 2\kappa^{-2}}{z\sqrt{4\kappa^{-2} - z^2}}. \tag{4}$$

The analytical solution of Eq. (4) is derived via complicated integration as

$$x = \kappa^{-1}\cosh^{-1}\left(\frac{2}{z\kappa}\right) - \sqrt{4\kappa^{-2} - z^2} + c_2, \tag{5}$$

where c_2 is an integration constant. The boundary condition $x=R\sin\theta$ at $z=h=\sqrt{2}\kappa^{-1}\sqrt{1+\cos(\theta+\theta_Y)}$ leads to:

$$c_2 = R\sin\theta - \kappa^{-1}\cosh^{-1}(2\kappa^{-1}/h) + 2\kappa^{-1}\sqrt{1-\kappa^2 h^2/4}. \tag{6}$$

B. Buoyant force and sinking condition

The buoyant force exerted on per unit length of the rod is proportional to the total volume of the extruded liquid, $V=V_1+V_2$, where V_1 stands for the volume of the wetted segment of the rod, and V_2 the volume of the dimple displaced by vapor. From Eq. (5) for a circular rod, we obtain

$$V_1 = R^2(\theta - \sin\theta\cos\theta),$$

$$V_2 = 2\int_0^h x dz = -2\kappa^{-2}\sin(\theta+\theta_Y) + 2\sqrt{2}\kappa^{-1}R\sin\theta\sqrt{1+\cos(\theta+\theta_Y)}. \tag{7}$$

Then the normalized buoyant force is written as a function of θ,

$$\tilde{F}_b = F_b\kappa^2/(\rho_L g) = \kappa^2 V, \tag{8}$$

as shown in Fig. 2, where we take $\theta_Y=120°$, and $\kappa^2R^2=0.25$, 0.01, and 0 for the three representative curves, respectively. When the cylinder radius R is very small (such as $\kappa^2R^2=0.01$), the buoyant force originates mainly from surface tension of the liquid (i.e., the first term of V_2), while for a larger R, the other terms of V associated with the volume of the rod itself also make a significant contribution. It is interesting to find from Fig. 2 that the buoyant force is not a monotonic function with increasing θ but has a maximum value at a certain angle, θ_{sink}. The buoyant force $\tilde{F}_b$ increases as θ increases in the range of $\theta < \theta_{\text{sink}}$, but decreases for a further increase of θ. In other words, the meniscus will become unstable when θ reaches to θ_{sink}. Therefore, the extremum condition of the buoyant force is that the volume of the displaced liquid, V, reaches its maximum. Then from $dV/d\theta=0$, one has

$$\sqrt{2}R\kappa^{-1}[2\sqrt{1+\cos(\theta+\theta_Y)}\cos\theta + \sqrt{1-\cos(\theta+\theta_Y)}\sin\theta] - 2\kappa^{-2}\cos(\theta+\theta_Y) + 2R^2\sin^2\theta = 0. \tag{9}$$

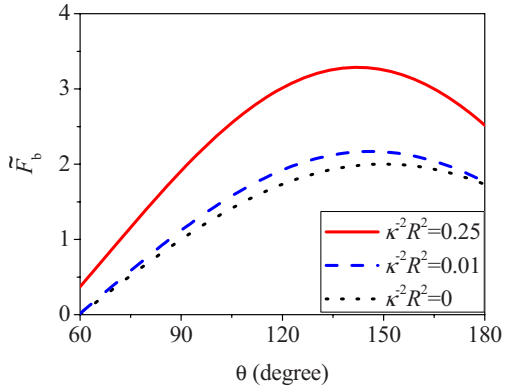

FIG. 2. (Color online) The variation of the nondimensional buoyant force with respect to the angle θ for three representative Bond numbers, κ^2R^2=0.25, 0.01, and 0.

Solution of this equation yields the critical value of θ at sinking, $\theta_{\text{sink}}^{(1)}$, and then the maximal buoyant force before sinking can be determined from Eqs. (7) and (8). This critical sinking condition of $dV/d\theta$=0 is called the maximal dimple-volume criterion or, for short, the volume criterion.

As aforementioned, the meniscus will have an inflection point when the angle θ is larger than $3\pi/2-\theta_Y$. In such a situation, one may also assume that the liquid surface will be pierced when the nearest distance of the two menisci approaches to zero. From Eq. (4) and using x'=0 (i.e., $z=\sqrt{2}\kappa^{-1}$), the minimum value of x of the meniscus at the right-hand side is expressed as

$$x_{\min} = \kappa^{-1}\cosh^{-1}(\sqrt{2}) - \sqrt{2}\kappa^{-1} + R\sin\theta - \kappa^{-1}\cosh^{-1}\left(\sqrt{\frac{2}{1+\cos(\theta+\theta_Y)}}\right) + \sqrt{2}\kappa^{-1}\sqrt{1-\cos(\theta+\theta_Y)}. \quad (10)$$

From $x_{\min}$=0 and Eq. (10), another critical value of θ at sinking, $\theta_{\text{sink}}^{(2)}$, can be determined. The critical sinking condition of $x_{\min}$=0 is referred to as the meniscus-contact condition or, for short, the distance criterion, which was used recently by Feng *et al.* [11] to calculate the buoyant force of a water strider leg.

Now we compare the two above sinking criteria. The critical states at sinking of the rod, in terms of θ_{sink}, and the corresponding nondimensional depth $\tilde{Z}_{\max}=\sqrt{2}\sqrt{1+\cos(\theta_{\text{sink}}+\theta_Y)}+R(1-\cos\theta_{\text{sink}})$ are calculated from both the volume condition $dV/d\theta$=0 or from the distance condition $x_{\min}$=0, as shown in Figs. 3(a) and 3(b), respectively. It is clear that the sinking angle and the corresponding depth of a rod predicted by the volume condition are always smaller than those by the distance condition, indicating that the maximum of the buoyant force is attained before the contact of the two menisci. When θ_Y=120°, for example, the volume condition predicts that the rod will sink at the sinking angle θ_{sink}=128.9° and the corresponding dimensionless rod depth is $\tilde{Z}_{\max}$=2.76, while the distance condition predicts θ_{sink}=168.7° and $\tilde{Z}_{\max}$=3.60. This indicates that the menisci have become unstable before their contact. Therefore, the

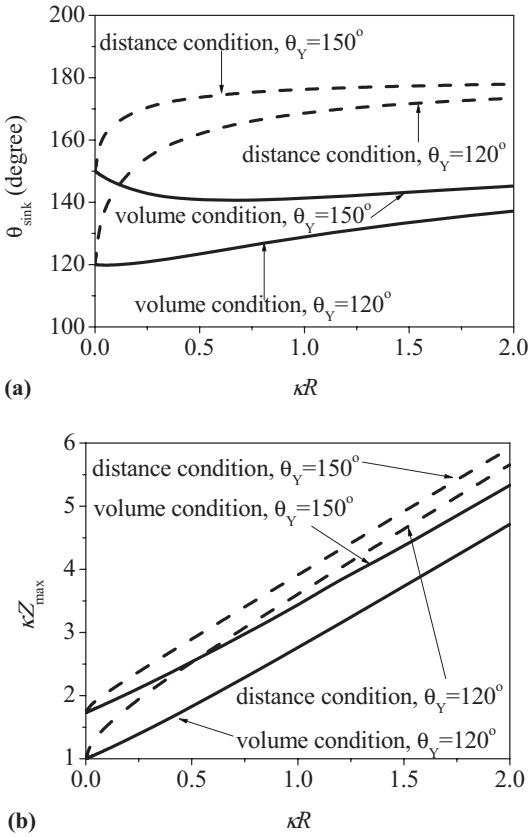

FIG. 3. Comparison of the maximal volume criterion and the meniscus-contact criterion. (a) The dependence of the sinking angle upon the rod radius, and (b) the dependence of the maximal depth upon the rod radius, where we take two representative Young's contact angles, θ_Y=120° and 150°.

volume criterion should always be used to determine when a hydrophobic circular rod will sink into the liquid. The meniscus-contact criterion, which has been adopted by Feng *et al.* [11] and some others, overestimates the dimple depth at sinking for a circular rod subjected to an increasing force.

In addition, it is worthy to rationalize the dependence of the maximal buoyant force upon the radius of the cylinder. For three representative radii of the rod, R=0.09 mm (a typical size of a water strider leg), 0.2 and 0.5 mm, the nondimensional maximal buoyant forces $\tilde{F}_{b\max}$ calculated from the above model are plotted in Fig. 4 as a function of the Young's contact angle θ_Y. For three representative Young's contact angles θ_Y=168° (the macroscopic contact angle of a water strider leg with hierarchical surface structures [11]), 120°, and 109° (corresponding to a smooth water strider leg coated with a wax layer), the nondimensional buoyant forces versus the rod radius are plotted in Fig. 5. Evidently, the maximal normalized buoyant force increases with the increase of either θ_Y or R. For a very thin rod, such as a water strider leg, $\tilde{F}_{b\max}$ increases slightly with the increase in θ_Y, while for a larger R, $\tilde{F}_{b\max}$ changes rapidly with θ_Y. In other words, the maximal buoyant force of a hydrophobic water strider leg is insensitive to its macroscopic Young's contact angle or its hierarchical surface structures. This conclusion is consistent with the numerical results of Vella *et al.* [32] and

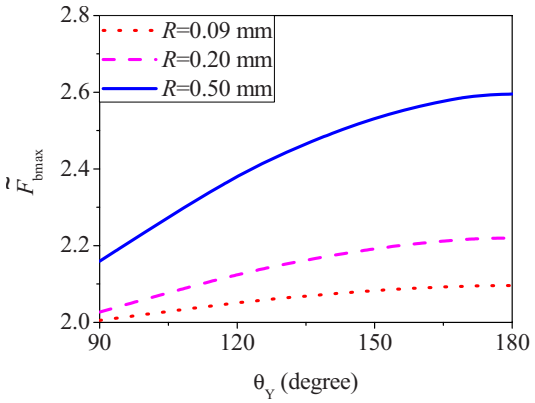

FIG. 4. (Color online) The dependence of the nondimensional maximal buoyant force upon the Young's contact angle, where we take $R=0.09$, 0.2, and 0.5 mm.

experimental measurements of Shi *et al.* [19]. The theoretical maximal buoyant force that a water strider leg can support is calculated here to be about 142 dynes, which is close to the experimental result of 152 dynes [10]. The slight difference is mainly due to the three-dimensional effect at the leg end, which has been neglected in our analytical solution. In spite of that, the hierarchical surface structure of the water strider leg does not make a significant contribution to the maximal buoyant force, fluid dynamics simulation reveals that it plays a key role in the propulsion process of the locomotive strider. The detailed analysis of the propelling mechanisms of water striders [2] is beyond the scope of the present paper.

C. Maximal radius and density of a rod that can float freely on water

Surface tension makes it possible that small objects with a mass density ρ_R higher than that of water can float freely on the liquid surface. The maximal radius $R_{\max}$ of a circular rod which the liquid can support is determined by equilibrating the maximal buoyant force $F_{b\,\max}$ with the rod weight $G=\rho_R g \pi R_{\max}^2$, that is,

$$F_{b\,\max} = \rho_L g V = G. \tag{11}$$

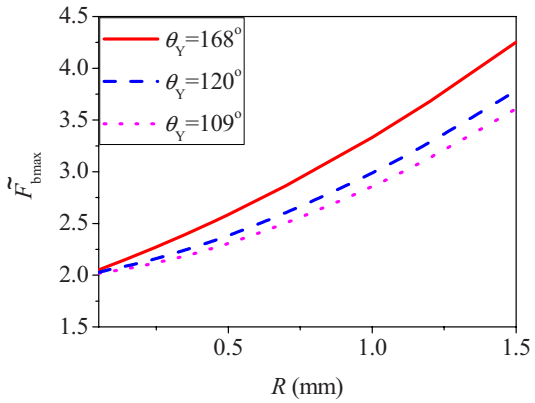

FIG. 5. (Color online) The dependence of the nondimensional maximal buoyant force upon the rod radius, where we take $\theta_Y=168°$, 120°, and 109°.

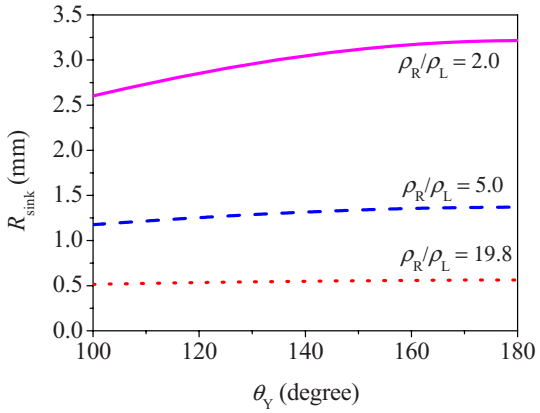

FIG. 6. (Color online) The dependence of the maximal radius upon the Young's contact angle for a freely floating rod, where we take three representative relative mass densities, $\rho_R/\rho_L=19.8$, 5.0, and 2.0.

Substituting Eqs. (7) and (8) into (11) leads to the following equation about $R_{\max}$:

$$(\rho_R/\rho_L)_{\max}\pi R_{\max}^2 = -2\kappa^{-2}\sin(\theta_{\sin k}+\theta_Y) + 2\sqrt{2}\kappa^{-1}R_{\max}\sin\theta_{\sin k}\sqrt{1+\cos(\theta_{\sin k}+\theta_Y)} + R_{\max}^2(\theta_{\sin k}-\sin\theta_{\sin k}\cos\theta_{\sin k}), \tag{12}$$

where the critical angle of sinking, $\theta_{\sin k}$, is also a function of $R_{\max}$. We solve Eq. (12) numerically.

The maximal radius for a rod floating freely on water can be calculated from the sinking condition $dV/d\theta=0$ and the equilibrium equation in Eq. (11), as shown in Fig. 6, where three representative relative densities $\rho_R/\rho_L=19.8$ (a gold rod), 5.0 and 2.0 have been chosen for illustration. The theoretical results are agreeable, in tendency, with the experimental data of Shi *et al.* [19], but their quantities have a slight difference. This may be attributed to the end effect, surface roughness and dynamic effect in the experiments.

For a specified Young's contact angle θ_Y and rod radius R, we can also determine from the above equations the maximal relative density of the rod $(\rho_R/\rho_L)_{\max}$ that can freely float. From Eqs. (9) and (11), the dependence relationship of the maximal relative density $(\rho_R/\rho_L)_{\max}$ and the Bond number κ^2R^2 is obtained, as shown in Fig. 7, which is consistent with the experimental results [32]. It is seen that the critical relative density decreases with the increase in the Bond number. This demonstrates that the liquid can support a denser rod with a thinner diameter. When $R=0.551$ mm and $\theta_Y=143°$, for example, water surface can bear a gold rod with a density of 19.8 g/mm^3, while for $R=1.0$ mm, a rod with a density larger than 2.4 g/mm^3 cannot float on water.

III. RODS OF DIFFERENT CROSS-SECTION SHAPES

A. Rod of an elliptical cross-section shape

In order to examine the dependence of the maximal buoyant force upon the cross-section shape, we now analyze floating rods of several special cross-section shapes. The elliptical cross section will be considered first, as shown in Fig.

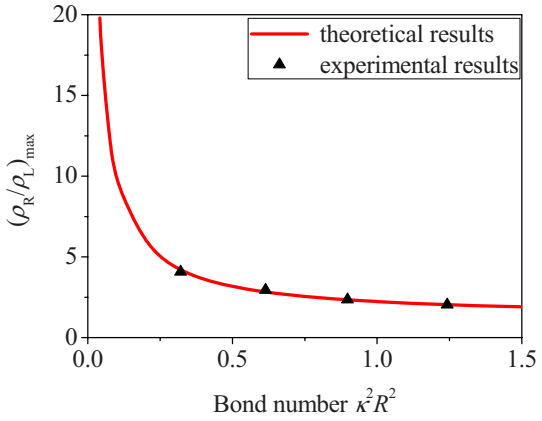

FIG. 7. (Color online) The maximal relative density of a circular rod that can float freely on water, where $\theta_Y=143°$ [32].

8(a), where $2a$ and $2b$ denote the main-axis lengths in the x and z directions, respectively, and the angle ϕ is measured from the vertical direction to the tangential direction of the liquid surface at the triple point. As in Sec. II A, an external force F is applied downwards to the rod of per unit length. The elliptical cross-section shape is expressed by

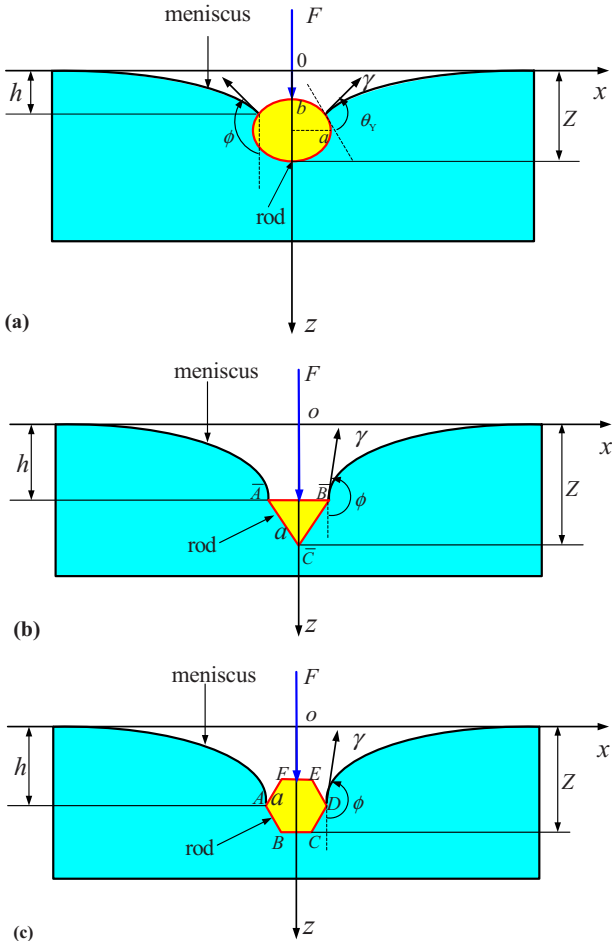

FIG. 8. (Color online) Rods with different cross sections floating on water surface: (a) elliptical, (b) triangular, and (c) hexagonal cross section.

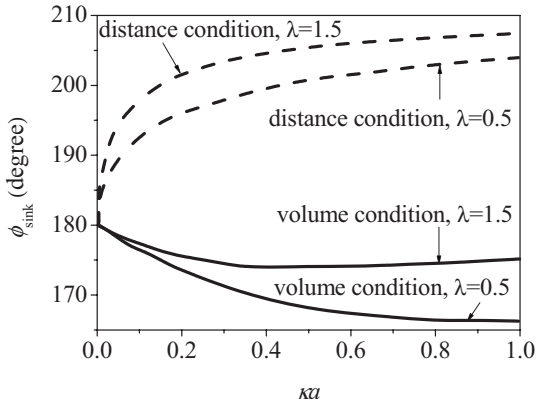

FIG. 9. The sinking angle of a rod of an elliptical cross section with respect to its normalized main axis length κa, where $\theta_Y=120°$, $\lambda=0.5$ and 1.5. The two sinking criteria based on the maximal dimple volume and the meniscus contact are compared.

$$\frac{x^2}{a^2}+\frac{(z+b-Z)^2}{b^2}=1, \tag{13}$$

where Z is the depth at the bottom of the rod [Fig. 8(a)]. One may easily prove the following geometric relation:

$$\sin(\phi-\theta_Y)=\frac{\lambda(\tilde{Z}-\tilde{b}-\tilde{z})}{\sqrt{(\lambda^2-1)(\tilde{Z}-\tilde{b}-\tilde{z})^2+\tilde{b}^2}}, \tag{14}$$

where the nondimensional parameters are defined as $\tilde{z}=\kappa z$, $\tilde{Z}=\kappa Z$, $\tilde{b}=\kappa b$, and $\lambda=a/b$.

Similar to Eq. (8) for a circular rod, the nondimensional buoyant force for an elliptical rod is derived as

$$\tilde{F}_b=-2\cos\phi+2\tilde{x}\sqrt{2(1-\sin\phi)}+\tilde{a}\tilde{b}\left(\frac{\pi}{2}+\arcsin\frac{\tilde{Z}-\tilde{b}-\tilde{z}}{\tilde{b}}\right.$$
$$\left.+\frac{\tilde{Z}-\tilde{b}-\tilde{z}}{\tilde{b}^2}\sqrt{\tilde{b}^2-(\tilde{Z}-\tilde{b}-\tilde{z})^2}\right), \tag{15}$$

where $\tilde{a}=\kappa a$ and $\tilde{x}=\kappa x$. Then the maximal buoyant force $\tilde{F}_{b\,max}$ can be determined from the sinking condition of the maximal volume, i.e., $dV/d\theta=0$.

For the elliptical rod, on the other hand, the connection condition of the two menisci, $x_{min}=0$, is recast as

$$\cosh^{-1}(\sqrt{2})-\sqrt{2}+\frac{\kappa a\lambda\cos(\phi-\theta_Y)}{\sqrt{1-(1-\lambda^2)\cos^2(\phi-\theta_Y)}}$$
$$-\cosh^{-1}\left(\sqrt{\frac{2}{1-\sin\phi}}\right)+\sqrt{2(1+\sin\phi)}=0. \tag{16}$$

The critical sinking states predicted from the two above conditions are plotted in Fig. 9 in terms of the critical angle ϕ_{sink} as a function of the size κa. It is seen that the sinking angle ϕ_{sink} predicted by the volume condition is always smaller than that of the meniscus-contact condition. Henceforth, the critical sinking condition of an elliptical rod subjected to an externally applied force F is always governed by the maximal volume condition. Therefore, the maximal

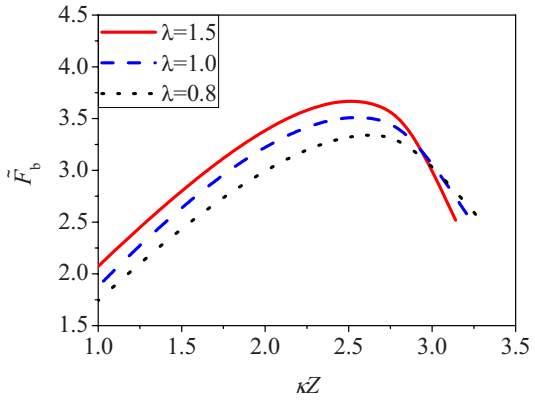

FIG. 10. (Color online) The nondimensional buoyant force as a function of the nondimensional depth of the rod with an elliptical cross-section shape, where $\theta_Y=120°$, $\lambda=1.5$, 1.0, and 0.8.

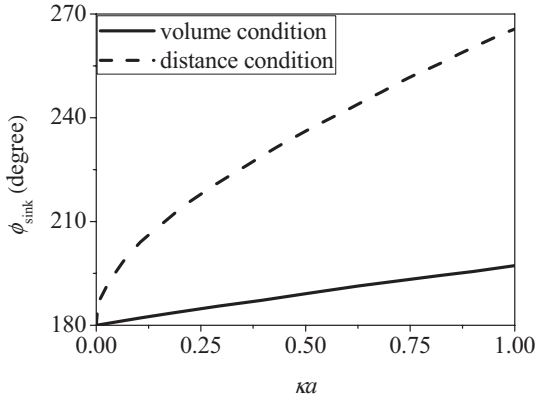

FIG. 11. The sinking angle of an equilateral triangular rod with respect to its normalized cross-section size κa, where we take $\theta_Y=120°$.

buoyant force should be determined from $dV/d\theta=0$, which is met before the linking of the two menisci.

From Eqs. (14)–(16), one may also give the dependence relationship between the buoyant force and the maximal depth of the elliptical rod, as shown in Fig. 10, where the nondimensional area of the elliptical cross section is $\pi ab\kappa^2=\pi/4$. With the increase in the ellipse aspect ratio $\lambda=a/b$, the maximal buoyant force $\tilde{F}_{b\,\max}$ of the rod increases. An elliptical rod with $\lambda>1$ can bear a bigger pressing force than a cylinder rod with the identical cross-sectional area.

B. Rod of an equilateral triangular cross-section shape

Now consider an equilateral triangular rod pressing a water surface, as shown in Fig. 8(b), where a is the side length of the cross section $\bar{A}\bar{B}\bar{C}$, and the angle ϕ is measured from the vertical direction to the tangential direction of the liquid surface at the triple point. A similar derivation leads to the expression of the nondimensional buoyant force $\tilde{F}_b$ as

$$\tilde{F}_b=-2\cos\phi+\frac{2\sqrt{6}}{3}(\tilde{Z}-\sqrt{2}\sqrt{1-\sin\phi})\sqrt{1-\sin\phi}+\frac{\sqrt{3}}{3}(\tilde{Z}-\sqrt{2}\sqrt{1-\sin\phi})^2, \tag{17}$$

where $\tilde{Z}=\kappa Z$ is the depth at point $\bar{C}$.

Equation (17) holds for both the cases when the triple point is located on the sides $\bar{A}\bar{C}$ and $\bar{B}\bar{C}$ or at the corners $\bar{A}$ and $\bar{B}$. For the former case, the contact lines move along the sides $\bar{A}\bar{C}$ and $\bar{B}\bar{C}$ and the depth varies in the range of $\sqrt{2(1-\sin\phi)}\le\tilde{Z}\le\sqrt{3}/2\tilde{a}+\sqrt{2(1-\sin\phi)}$, where $\phi=\theta_Y-30°$. While for the latter, the angle ϕ is variable in the range $\theta_Y-30°\le\phi\le\theta_Y+90°$ (Gibbs inequality [35]) due to the curvature singularity, and the depth of the rod is expressed as $\tilde{Z}=\sqrt{3}/2\tilde{a}+\sqrt{2(1-\sin\phi)}$. The maximal dimple-volume condition (i.e., $dV/d\theta=0$) and the contact condition of two menisci (i.e., $x_{\min}=0$), respectively, yields

$$\tilde{a}=-\frac{2\sqrt{2}\sin\phi_{sink}}{\sqrt{1+\sin\phi_{sink}}}, \tag{18}$$

$$\tilde{a}=2\cosh^{-1}\left(\sqrt{\frac{2}{1-\sin\phi_{sink}}}\right)-2\sqrt{2(1+\sin\phi_{sink})}+2\sqrt{2}-2\cosh^{-1}(\sqrt{2}). \tag{19}$$

The dependence relationship between ϕ_{sink} and $\tilde{a}$ is plotted in Fig. 11. It is again concluded that the maximal buoyant force of the rod is governed by the maximal volume condition.

From Eq. (17), the nondimensional buoyant force of the rod is given as a function of its depth $\tilde{Z}$ in Fig. 12, where the Young's contact angle is taken as 120° and 150° for the two curves, respectively, and the cross-sectional area of the rod, normalized by κ^{-2}, is $\pi/4$. It is seen that with the increase in θ_Y, the maximal buoyant force increases. At the corner $\bar{B}$, the curves are not smooth because of the Gibbs inequality relation.

C. Rod of a hexagonal cross-section shape

Another representative but more complicated example is a floating rod with a hexagonal cross section of the side length a, as shown in Fig. 8(c). The external force F and the angle ϕ are defined the same as in Sec. III A. According to the locations of the contact lines, the pressing process of a hydrophobic hexagonal rod on water can generally be divided into the following five stages.

(i) If $\theta_Y>120°$, once the rod contacts the water surface, the left and the right contact lines will first be pinned at the corners B and C, respectively. In this stage, the corresponding boundary conditions are $90°\le\phi\le\theta_Y-30°$, $\tilde{x}=\tilde{a}/2$, and $\tilde{Z}=\sqrt{2(1-\sin\phi)}$, where $(\tilde{x},\tilde{Z})$ are the coordinates of the right contact line. If $\theta_Y\le120°$, however, the contact lines cannot be pinned at the corners B and C since the Gibbs inequality cannot be met, and therefore this stage does not exist.

(ii) The contact line moves along the sides AB and CD as the force F increases. In this stage, simple geometric analysis leads to $\phi=\theta_Y-30°$ and $\tilde{x}=(\tilde{a}/2)+(1/\sqrt{3})[\tilde{Z}-\sqrt{2(1-\sin\phi)}]$.

(iii) After arriving the corners A and D, the contact lines will be pinned there in the range of $\theta_Y-30°\le\phi\le\theta_Y+30°$,

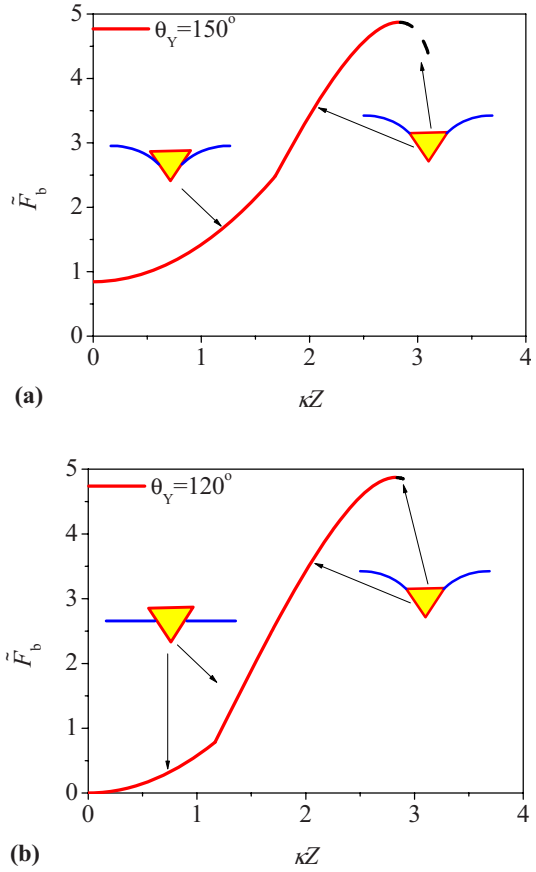

FIG. 12. (Color online) The variation of the nondimensional buoyant force with respect to the nondimensional depth for an equilateral triangular rod with (a) $\theta_Y=150°$, and (b) $\theta_Y=120°$.

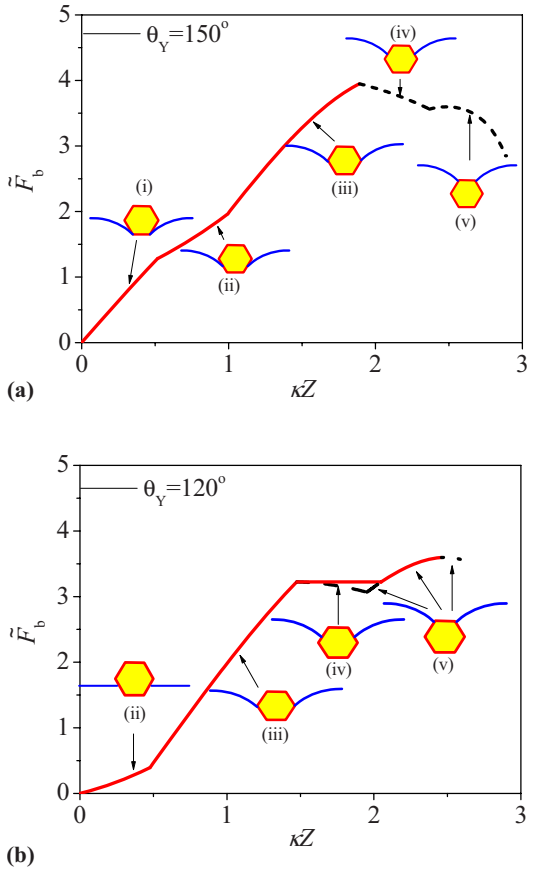

FIG. 13. (Color online) The variation of the nondimensional buoyant force with respect to nondimensional depth for a hexagon rod with (a) $\theta_Y=150°$, and (b) $\theta_Y=120°$.

during which stage one has $\tilde{x}=\tilde{a}$ and $\tilde{Z}=\sqrt{2(1-\sin\phi)}+(\sqrt{3}/2\tilde{a})$.

(iv) The two contact lines move along the sides AF and DE, respectively. In this regime, we have $\phi=\theta_Y+30°$ and $\tilde{x}=(3\tilde{a}/2)-(1/\sqrt{3})[\tilde{Z}-\sqrt{2(1-\sin\phi)}]$.

(v) Finally, the contact lines may be pinned again at the corners E and F. Correspondingly, the boundary conditions are $\theta_Y+30°\leq\phi\leq\theta_Y+90°$, $\tilde{x}=\tilde{a}/2$, and $\tilde{Z}=\sqrt{2(1-\sin\phi)}+\sqrt{3}\tilde{a}$.

The nondimensional buoyant force can be calculated by

$$\tilde{F}_b=-2\cos\phi+2\tilde{x}\sqrt{2(1-\sin\phi)}+\frac{1}{\sqrt{3}}[\tilde{Z}-\sqrt{2(1-\sin\phi)}]\times[\sqrt{3}\tilde{a}+\tilde{Z}-\sqrt{2(1-\sin\phi)}] \quad (20)$$

in stages (i)–(iii), or by

$$\tilde{F}_b=-2\cos\phi+2\tilde{x}\sqrt{2(1-\sin\phi)}+\frac{\pi}{8}+\left(\tilde{Z}-\sqrt{2(1-\sin\phi)}-\frac{\sqrt{3}\tilde{a}}{2}\right)\left[2\tilde{a}-\frac{\sqrt{3}}{3}\left(\tilde{Z}-\sqrt{2(1-\sin\phi)}-\frac{\sqrt{3}\tilde{a}}{2}\right)\right], \quad (21)$$

in stages (iv) and (v).

For $\theta_Y=150°$, for example, the changing curve of the buoyant force $\tilde{F}_b$ with the rod depth $\tilde{Z}=\kappa Z$ is shown in Fig. 13(a), where the nondimensional area cross section of the rod is $\pi/4$. The solid and dashed curves stand for stable and unstable floating states. Here a state is called unstable when the rod cannot bear any further increase in the externally applied force F, or, in other words, the function $\tilde{F}_b(\tilde{Z})$ is decreasing. In stages (i)–(iii), the buoyant force of the rod increases with the depth, and the rod can bear an increasing pressing force F; while stages (iv) and (v) are unstable. Therefore, the maximal buoyant force, which is achieved at the end of stage (iii), can be calculated from Eq. (20) by setting $\phi=180°$. After that, the rod will sink into water.

For a special contact angle $\theta_Y=120°$, the buoyant force curve is shown in Fig. 13(b). In this case, the contact lines cannot be pinned at the corners B and C, and the buoyant force curve in stage (i) shrinks to a point. With the increase in the pressing force, the contact lines remain horizontal ($\phi=90°$) and move along the sides AB and CD. The following stages (iii) and (iv) are similar to those for $\theta_Y=150°$, but stage (v) is stable in a certain range of ϕ. The triple lines will jump rapidly from the corners A and D to F and E. Therefore, the buoyant force will reach its maximum in stage (v) before the loss of its stability. Our analysis demonstrates that the sinking condition for a hexagonal rod is still governed by the maximal dimple-volume criterion.

TABLE I. Comparisons of the maximal buoyant forces of rods with different cross-section shapes, where their nondimensional cross-sectional areas are all taken as $\pi/4$, and the Young's contact angle $\theta_Y=120°$.

Cross-section shape	Maximal buoyant force
Ellipse ($\lambda=0.8$)	3.3591
Ellipse ($\lambda=1.0$)	3.5303
Ellipse ($\lambda=1.5$)	3.6807
Annulus	4.3997
Equilateral triangle	4.8728
Hexagon	3.6118

D. Comparisons of the maximal buoyant forces for different cross-section shapes

The above method also applies to several other cases, such as the triangular shapes with the tip down and hexagonal shapes with flat sides up, and they may be analyzed similarly. The maximal buoyant forces of thin and long rods with different cross-section shapes are compared in Table I, where their nondimensional cross-sectional areas are all taken as $\pi/4$, and the Young's contact angle $\theta_Y=120°$. The formulas for a rod with an annular cross section are identical to those for a circular rod in Sec. II. It is found that the annular and the equilateral triangular cross sections produce larger buoyant forces than the four others listed in the table.

IV. OPTIMIZATION MECHANISMS OF WATER STRIDER LEGS

Through evolution of many millions of years, such creatures as water striders and water spiders have gained the striking ability to live on water. For instance, experimental measurements [10,11] found that a single water strider leg can hold a force about 15 times the total weight of the insect's body without piercing the water surface. In this section, the above theoretical results will be used to illustrate how a water strider leg achieves a so large buoyant force. Based on our above analysis on buoyant forces, its optimization mechanisms are summarized as follows.

First, scanning electron microscopic observations clearly revealed that a water strider leg are covered with a large number of tiny chitinous setae, which are oriented at an inclined angle of about 20° measured from the leg surface [10,11,36,37]. These needlelike setae are about 50 μm in length and less than 3 μm in diameter, and, more interestingly, their surfaces have some elaborate nanosized grooves. Such hierarchical microstructures and nanostructures, in conjunction with the secreted wax coating on the leg surface, render a contact angle larger than 150°, which plays a key role in the propulsion process of the locomotive strider.

Second, the special cross-section shape of the water strider leg also makes a considerable contribution to the large buoyant force. In fact, its cross section is not a solid circular shape but a hollow or annular one. For a given material mass, the annular shape will have a larger diameter and a higher bending strength than a solid circular shape. As concluded in Sec. II B, the maximal buoyant force of a circular or annular rod is sensitively dependent upon its diameter. According to experimental observations, the outer radius is about 1.5 times the inner. For the same nondimensional cross-sectional area of $\pi/4$, the nondimensional maximal buoyant forces are 4.40 for the annular rod and 3.53 for the solid circular rod. Therefore, the annular cross-section shape of the water strider leg is an optimized one from the angles of low mass density, high bending strength, and large buoyant force. It should also be mentioned that under a given cross-sectional area, the maximal outer radius of a water strider leg is limited by its instability since local buckling is apt to happen in a thin shell under bending. Analysis of the strength and instability of water strider legs are beyond the scope of the present paper.

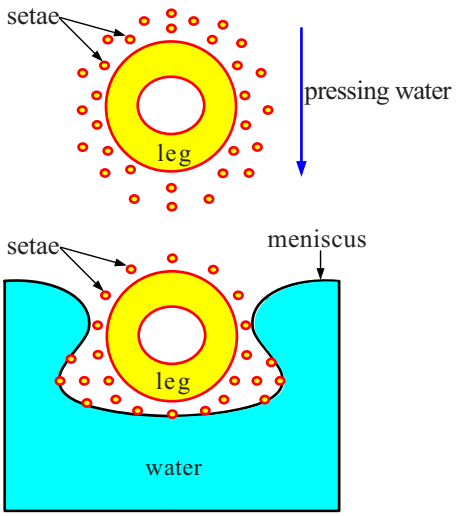

FIG. 14. (Color online) A water strider leg pressing a water surface. The elastic deformation renders a bigger contact width between the leg and the water surface, resulting in a further enhancement of the repellency behavior of the leg.

Additionally, the adaptive elastic deformation of a water strider leg with two flexible joints also contributes to the increase of its buoyant force. As aforementioned, the leg has a large number of setae, which are equivalent to a soft layer outside the leg. Before its contact with the water surface, the leg has a hollow annular shape, but when subjected to a downward pressing force, it will deform into a self-adaptive shape, as shown in Fig. 14. Our above calculation shows that such a deformed shape is able to create a higher buoyant force.

The above analysis evidences that a water strider leg can achieve an extremely higher buoyant force by several distinctly different mechanisms, including (i) the hierarchical microstructures and nanostructures with a wax coating, which lead to the superhydrophobic surface property or a large Young's contact angle, (ii) the hollow annular cross-section shape, which increases the leg diameter, and (iii) the elastic deformation, which serves as a further enhancement of the repelling ability. Furthermore, the two flexible joints connecting the three segments of the leg also help prevent its piercing into water [38]. These mechanisms provide inspirations for design of innovative miniature aquatic devices and nonwetting materials.

V. CONCLUSIONS

Motivated by the observation of the striking repellency behavior of such creatures as water striders and water spiders living on water, the buoyant force of a floating thin rod has been theoretically investigated in this paper. The shape function of the meniscus and the induced buoyant force are derived analytically for a hydrophobic long rod with different cross-section shapes. The sinking conditions of the maximal volume condition ($dV/d\theta=0$) and the meniscus-contact condition ($x_{\min}=0$) are discussed in detail. It is found that the latter criterion overestimates the maximal depth of the rod, and, therefore, the maximal pressing force a rod can bear should always be determined from the maximal volume condition. The maximal buoyant force increases with increasing the Young's contact angle and the rod radius. The theoretical result is consistent with numerical and experimental results. We have also examined the dependence of the maximal buoyant force on the cross-section shape by comparing the rods of several typical shapes. It should be mentioned that the adopted method based on force and geometry analysis is equivalent to the energy method [39].

It is interesting to find that to achieve an extremely strong ability to live on water, a water strider leg has several distinctly different mechanisms, including the hierarchical microstructures and nanostructures with a wax coating, the hollow annular cross-section shape, and the elastic deformation. These mechanisms provide inspirations for design of innovative miniature aquatic devices and nonwetting materials from different aspects (e.g., geometric shape, characteristic size, surface microstructure, and elasticity).

ACKNOWLEDGMENTS

The support from the National Natural Science Foundation of China (Grants Nos. 10732050, 10525210, 10602042, and 10121202) is acknowledged.

[1] R. S. Wilcox, Science **206**, 1325 (1979).
[2] J. W. M. Bush and D. L. Hu, Annu. Rev. Fluid Mech. **38**, 339 (2006).
[3] D. L. Hu and J. W. M. Bush, Nature (London) **437**, 733 (2005).
[4] R. B. Suter and H. Wildman, J. Exp. Bot. **202**, 771 (1999).
[5] R. B. Suter, O. Rosenberg, S. Loeb, S. H. Wildman, and J. H. Long, J. Exp. Bot. **200**, 2523 (1997).
[6] R. B. Suter, G. E. Stratton, and P. R. Miller, J. Arachnol. **31**, 428 (2003).
[7] R. B. Suter, G. E. Stratton, and P. R. Miller, J. Arachnol. **32**, 11 (2004).
[8] M. Dickinson, Nature (London) **424**, 621 (2003).
[9] D. L. Hu, B. Chan, and J. W. Bush, Nature (London) **424**, 663 (2003).
[10] X. F. Gao and L. Jiang, Nature (London) **432**, 26 (2004).
[11] X. Q. Feng, X. F. Gao, Z. N. Wu, L. Jiang, and Q. S. Zheng, Langmuir **23**, 4892 (2007).
[12] P. G. de Gennes, Rev. Mod. Phys. **57**, 827 (1985).
[13] C. Yang, U. Tartaglino, and B. N. J. Persson, Phys. Rev. Lett. **97**, 116103 (2006).
[14] J. L. Liu, X. Q. Feng, G. F. Wang, and S. W. Yu, J. Phys.: Condens. Matter **19**, 356002 (2007).
[15] C. W. Wu, X. Q. Kong, and D. Wu, Phys. Rev. E **76**, 017301 (2007).
[16] C. Neinhuis and W. Barthlott, Ann. Bot. (London) **79**, 667 (1997).
[17] A. Otten and S. Herminghaus, Langmuir **20**, 2405 (2004).
[18] N. Zhao, F. Shi, Z. Q. Wang, and X. Zhang, Langmuir **21**, 4713 (2005).
[19] F. Shi, Z. Q. Wang, and X. Zhang, Adv. Mater. **17**, 1005 (2005).
[20] F. Shi, J. Niu, J. L. Liu, F. Liu, Z. Q. Wang, X. Q. Feng, and X. Zhang, Adv. Mater. **19**, 2257 (2007).
[21] C. Clanet and D. Quere, J. Fluid Mech. **460**, 131 (2002).
[22] T. Podgorski and A. Belmonte, Eur. J. Appl. Math. **15**, 385 (2004).
[23] G. I. Taylor and D. H. Michael, J. Fluid Mech. **58**, 625 (1973).
[24] J. B. Keller, Phys. Fluids **10**, 3009 (1998).
[25] G. M. Whitesides and B. Grzybowski, Science **295**, 2418 (2002).
[26] D. Vella, P. D. Metcalfe, and R. J. Whittaker, J. Fluid Mech. **549**, 215 (2006).
[27] J. L. Trompette, S. Rouaix, and D. Amaro-Gonzalez, Powder Technol. **132**, 154 (2003).
[28] A. R. Penner, Am. J. Phys. **68**, 549 (2000).
[29] A. V. Rapacchietta, A. W. Neumann, and S. N. Omenyi, J. Colloid Interface Sci. **59**, 541 (1977).
[30] A. V. Rapacchietta, A. W. Neumann, and S. N. Omenyi, J. Colloid Interface Sci. **59**, 555 (1977).
[31] T. I. Hesla and D. D. Joseph, J. Colloid Interface Sci. **279**, 186 (2004).
[32] D. Vella, D. G. Lee, and H. Y. Kim, Langmuir **22**, 5979 (2006).
[33] P. Singh and D. D. Joseph, J. Fluid Mech. **530**, 31 (2005).
[34] A. W. Adamson, *Physical Chemistry of Surfaces* (Wiley, New York, 1990).
[35] D. Quere, Physica A **313**, 32 (2002).
[36] L. Cheng, Nature (London) **242**, 132 (1973).
[37] N. M. Andersen, Vidensk. Meddr. Dansk. Naturh. Foren. **139**, 337 (1976).
[38] Q. S. Zheng and Y. Yu (unpublished).
[39] S. Q. Huang, Q. Y. Li, X. Q. Feng, and S. W. Yu, Mech. Mater. **38**, 88 (2006).